JACS
JOURNAL OF THE AMERICAN CHEMICAL SOCIETY

Article

pubs.acs.org/JACS

Donor–Acceptor Interaction Determines the Mechanism of Photoinduced Electron Injection from Graphene Quantum Dots into TiO_2: π-Stacking Supersedes Covalent Bonding

Run Long,*[,†] David Casanova,[‡,§] Wei-Hai Fang,[†] and Oleg V. Prezhdo*[,∥]

[†]College of Chemistry, Key Laboratory of Theoretical & Computational Photochemistry of Ministry of Education, Beijing Normal University, Beijing, 100875, P. R. China

[‡]Kimika Fakultatea, Euskal Herriko Unibertsitatea and Donostia International Physics Center, 20018 Donostia, Euskadi, Spain

[§]IKERBASQUE, Basque Foundation for Science, 48013 Bilbao, Euskadi, Spain

[∥]Department of Chemistry, University of Southern California, Los Angeles, California 90089, United States

Supporting Information

ABSTRACT: Interfacial electron transfer (ET) constitutes the key step in conversion of solar energy into electricity and fuels. Required for fast and efficient charge separation, strong donor–acceptor interaction is typically achieved through covalent chemical bonding and leads to fast, adiabatic ET. Focusing on interfaces of pyrene, coronene, and a graphene quantum dot (GQD) with TiO_2, we demonstrate the opposite situation: covalent bonding leads to weak coupling and nonadiabatic (NA) ET, while through-space π-electron interaction produces adiabatic ET. Using real-time time-dependent density functional theory combined with NA molecular dynamics, we simulate photoinduced ET into TiO_2 from flat and vertically placed molecules and GQD containing commonly used carboxylic acid linkers. Both arrangements can be achieved experimentally with GQDs and other two-dimensional materials, such as MoS_2. The weak through-bond donor–acceptor coupling is attributed to the π-electron withdrawing properties of the carboxylic acid group. The calculated ET time scales are in excellent agreement with pump–probe optical experiments. The simulations show that the ET proceeds faster than energy relaxation. The electron couples to a broad spectrum of vibrational modes, ranging from 100 cm^{-1} large-scale motions to 1600 cm^{-1} C–C stretches. Compared to graphene/TiO_2 heterojunctions, the molecule/TiO_2 and GQD/TiO_2 systems exhibit energy gaps, allowing for longer-lived excited states and hot electron injection, facilitating charge separation and higher voltage. The reported state-of-the-art simulations generate a detailed time-domain, atomistic description of the interfacial charge and energy transfer and relaxation processes, and demonstrate that the fundamental principles leading to efficient charge separation in nanoscale materials depend strongly and often unexpectedly on the type of donor–acceptor interaction. Understanding these principles is critical to the development of highly efficient photovoltaic and photocatalytic cells.

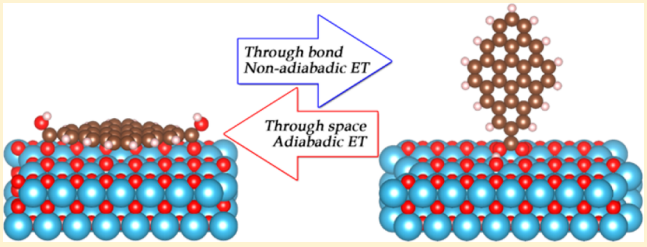

1. INTRODUCTION

A two-dimensional form of carbon, graphene is composed of a planar hexagonal lattice of carbon atoms with a C–C bond length of 1.42 Å. The atoms are connected by both σ-bonds formed by sp^2-electrons and π-bonds formed by p_z-electrons. These chemical features endow graphene with many unique properties, such as high electron and hole mobilities,[1,2] leading to very high thermal and electronic conductivities,[3−5] and large surface area per unit of mass[6] (up to ∼2600 m^2/g). Graphene attracts intense attention for a diverse range of applications, including photocatalysis[7−12] and photovoltaics.[13−15] Small finite-size pieces of graphene are known as graphene quantum dots (GQDs). In addition to the unique properties inherited from graphene, such as high surface area and single atom thickness, GQDs exhibit size behavior. In particular, graphene is a metal, while GQDs have a size-dependent energy gap, which can be tuned to absorb solar photons of any wavelength, from near-infrared, to visible, to ultraviolet. The presence of the energy gap itself, which ensures long-lived excited states, and the gap tunability are strongly desirable in solar energy applications. One can use GQDs to fabricate solar cells directly[16,17] or employ them as photosensitizers interfaced with metal oxides and giving rise to visible-light photocatalytic and photovoltaic devices.[18]

Composites of nanoscale carbon materials with TiO_2, including carbon nanotubes, graphene, and GQDs, are attracting significant attention in photovoltaics and photocatalysis, because these systems harvest a broad spectrum of solar light and exhibit fast charge separation.[18,19] A number of factors make GQDs preferable to graphene and nanotubes. Compared to metallic graphene, GQDs have discrete electronic

Received: September 13, 2016
Published: January 26, 2017

DOI: 10.1021/jacs.6b09598
J. Am. Chem. Soc. 2017, 139, 2619–2629

levels, allowing for hot electron injection and efficient charge separation. Both experiment[17] and theory[20] demonstrate 10–100 ps hot electron lifetimes in GQDs. Compared to nanotubes, all of the GQD extended π-electron systems can be put in direct contact with a TiO_2 surface, facilitating the donor–acceptor contact. Quantum confinement can increase the electronic coupling between GQDs and TiO_2. The coupling can be enhanced further by covalent linking between GQD and TiO_2 through a variety of functional groups available due to the versatile chemistry of the carbon atom.[21]

Zhu and co-workers reported sub-15 fs electron injection from GQDs to TiO_2, using pump–probe optical measurements.[18] The transfer from GQDs is faster than that from graphene.[19] The ultrafast photoinduced electron injection results in efficient spatial separation of electrons and holes, and reduces their geminate recombination.[17] The experiments show fast and slow recombination time scales, the latter being strongly dependent on excitation photon energy. The fast time scale is attributed to prompt recombination of the electron and hole bound at the interface. The excitation energy dependence of the slow channel arises due to hot electron injection from GQDs to TiO_2. The gaps between GQD excited electronic states[20] create a phonon bottleneck[17] to the electron–phonon energy exchange, making injection faster than relaxation. Hot injected electrons travel into the TiO_2 bulk, and only later return to the interface and recombine with holes. Electron–phonon energy exchange often results in low charge separation efficiency, leading to an undesired loss of the photogenerated electrons due to charge trapping on QD surfaces and charge recombination during transport through the semiconductor oxide substrate.[22] The ultrafast sub-15 fs electron injection from photoexcited GQDs into TiO_2 indicates that GQD/TiO_2 composites can yield high photo-to-electron conversion, because the charge separation at the interface is fast and efficient. This finding provides a strong motivation for modeling of the charge separation dynamics at GQD/TiO_2 interfaces, in order to develop a thorough understanding of the dynamics and its mechanisms, and to provide chemical guidelines for the development of GQD/TiO_2 solar cells.

At present, we report time-domain ab initio simulations of the photoinduced electron injection to TiO_2 from pyrene, coronene, and a GQD that are covalently linked to the TiO_2 surface in either flat (F-pyrene, F-coronene) or vertical (V-pyrene, VGQD) configurations, Figure 1. The flat arrangement allows for through-space interaction of π-electrons with the semiconductor surface. Such interaction is absent in the vertical systems. Surprisingly, covalent bonding through the short carboxylic acid group, a commonly used linker, does not provide a sufficiently strong donor–acceptor coupling, leading to the NA ET mechanism that operates in the weak coupling limit. This observation is rationalized by the π-electron withdrawing properties of the carboxylic group, and should apply to other commonly used linkers. At the same time, the through-space coupling via π-electron stacking is strong, leading to the adiabatic ET. The findings contradict the general expectation that strong donor–acceptor coupling requires covalent bonding. In both cases, the injection is ultrafast, in excellent agreement with the experimental data. Photoexcitation of molecules and GQD leads to partially charge-separated states, with the charge-transfer character decreasing with increasing GQD size. The ET and energy transfer are consistently faster than energy relaxation, allowing for injection of hot, unrelaxed electrons. A detailed analysis of the simulation

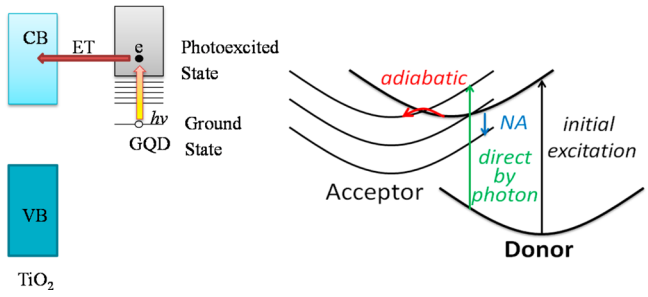

Figure 1. Schematic of the photoinduced electron injection from a GQD into a TiO_2 surface (left panel). An absorbed photon promotes an electron from the GQD ground state with energy inside the TiO_2 band gap, into an excited state that is in resonance with the TiO_2 conduction band (CB). The excited electron is injected into the TiO_2 CB via several mechanisms (right panel). The GQD donor can transfer the electron to the TiO_2 acceptor either adiabatically by passing over a transition state barrier (curved red arrow) or nonadiabatically via a hop between donor and acceptor states (vertical blue arrow). Additionally, the electron can be promoted from donor to acceptor during the photoexcitation process.

data rationalizes the difference between the through-bond and through-space donor–acceptor interactions in the GQD/TiO_2 composites. Applicable to other systems, the reported design principles demonstrate how the properties of solar cells and electronic devices can be controlled by orientation and binding chemistry.

2. THEORETICAL METHODOLOGIES

The time-domain atomistic simulations of the photoinduced electron injection from the donor species (pyrene, coronene, and GQD) into the TiO_2 acceptor are performed by an approach[23] combining NA molecular dynamics (NAMD) with ab initio real-time time-dependent density functional theory (TD-DFT). Fewest switches surface hopping (FSSH)[24] is formulated in the Kohn–Sham representation[23,25] and adapted to the classical path approximation.[26] In this mixed quantum-classical technique, the electrons are treated quantum mechanically, while the nuclei are classical.[27] The approach has been applied previously to study ET and relaxation dynamics at the interfaces of inorganic semiconductors with molecular chromophores,[28−32] semiconductor QDs,[33−36] graphene,[37] metallic nanoparticles,[38] water,[39] organic/inorganic perovskites,[40−43] etc.[44−54] The approach mimics the pump–probe optical experiments in the most direct way, and provides an atomistic description of chemical and physical processes and interactions in real time. The details of the methodology can be found elsewhere.[26,55] The following subsections provide a brief introduction to the TDDFT-NAMD methodology and computational procedure.

2.1. Time-Dependent Kohn–Sham Theory for Electron–Nuclear Dynamics. The ET dynamics including the NA effects[56] are described by TD-DFT[25,57] with the Kohn–Sham (KS) approach.[58] The electron density at time t, $\rho(\mathbf{r}, t)$, is expressed by the sum of the overall densities of the occupied single-electron KS orbital

$$\rho(\mathbf{r}, t) = \sum_{p=1}^{N_e} |\varphi_p(\mathbf{r}, t)|^2 \quad (1)$$

DOI: 10.1021/jacs.6b09598
J. Am. Chem. Soc. 2017, 139, 2619–2629

where $p = 1, 2, ..., N_e$ and N_e is the number of electrons. The evolution of the electron density is determined by the TD variational principle applied to the KS energy:

$$E\{\varphi_p\} = \sum_{p=1}^{N_e} \langle \varphi_p | K(\mathbf{r}) | \varphi_p \rangle + \sum_{p=1}^{N_e} \langle \varphi_p | V(\mathbf{r}; \mathbf{R}) | \varphi_p \rangle + \frac{e^2}{2} \iint \frac{\rho(\mathbf{r}', t)\rho(\mathbf{r}, t)}{|\mathbf{r} - \mathbf{r}'|} \, d^3\mathbf{r} \, d^3\mathbf{r}' + E_{XC}\{\rho\} \quad (2)$$

Here, the first, second, third, and fourth terms on the right-hand side represent the kinetic energy of noninteracting electrons, the electron−nuclear attraction, the electron−electron Coulomb repulsion, and the exchange-correlation energy functional, respectively. With proper selection of exchange-correlation functionals, DFT is capable of describing various properties of complex systems in the scope of physics, chemistry, biology, and material sciences. Application of the TD variational principle to eq 2 leads to a set of single-particle equations for the evolution of KS orbitals.[58,59]

$$i\hbar \frac{\partial \varphi_p(\mathbf{r}, t)}{\partial t} = H(\mathbf{r}, \mathbf{R}, t)\varphi_p(\mathbf{r}, t) \quad (3)$$

The equations are coupled because the DFT Hamiltonian $H(\mathbf{r}, \mathbf{R}, t)$ depends on the overall electron density. The electron-vibrational interactions enter the Hamiltonian through the external potential created by the nuclei. The TD single-electron orbitals in eq 3 are expressed on the basis of the adiabatic KS orbitals, $\tilde{\varphi}_k(\mathbf{r}, \mathbf{R}(t))$, which are calculated for the current atomic positions $\mathbf{R}$. The focus is on the evolution of the orbital $\varphi_{photoexcited}(\mathbf{r}, t)$ occupied by the photoexcited electron. As demonstrated previously,[29,30,33,37−39] the ET dynamics at chromophore/TiO_2 interfaces are well described by the evolution of the photoexcited electron, which involves unoccupied orbitals of the molecules, GQD, and TiO_2 conduction band states.

$$\varphi_{photoexcited}(\mathbf{r}, t) = \sum_{k=1}^{N_e} c_k(t) | \tilde{\varphi}_k(\mathbf{r}, \mathbf{R}(t)) \rangle \quad (4)$$

Insertion of eq 4 into eq 3 generates a set of equations describing the evolution of the expansion coefficients:

$$i\hbar \frac{\partial}{\partial t} c_j(t) = \sum_{k}^{N_e} c_k(t)(\varepsilon_k \delta_{jk} + \mathbf{d}_{jk} \cdot \dot{\mathbf{R}}) \quad (5)$$

Here, ε_k is the energy of the adiabatic state k and $\mathbf{d}_{jk} \cdot \dot{\mathbf{R}}$ is the NA coupling between orbitals k and j, generated by atomic motions. We calculated the NA coupling numerically as the overlap of orbitals j and k at sequential time steps[60]

$$\begin{aligned} \mathbf{d}_{jk} \cdot \dot{\mathbf{R}} &= -i\hbar \langle \tilde{\varphi}_j(\mathbf{r}, \mathbf{R}(t)) | \nabla_R | \tilde{\varphi}_k(\mathbf{r}, \mathbf{R}(t)) \rangle \cdot \dot{\mathbf{R}} \\ &= -i\hbar \left\langle \tilde{\varphi}_j(\mathbf{r}, \mathbf{R}(t)) \left| \frac{\partial}{\partial t} \right| \tilde{\varphi}_k(\mathbf{r}, \mathbf{R}(t)) \right\rangle \\ &\approx -\frac{i\hbar}{2\Delta t} (\langle \phi_j(t) | \phi_k(t + \Delta t) \rangle - \langle \phi_j(t + \Delta t) | \phi_k(t) \rangle) \end{aligned} \quad (6)$$

2.2. Electron Transfer Mechanisms. The extent of ET from the molecules and GQD to the TiO_2 surface is computed by integrating the photoexcited electron density over the region of the simulation cell occupied by F-pyrene, F-coronene, V-pyrene, and VGQD, and subtracting it from 1 to obtain the density localized on the acceptor, Figure 2:

$$\begin{aligned} &\int_{donor} \rho_{photoexcited}(\mathbf{r}, t) \, d\mathbf{r} \\ &= \int_{donor} |\varphi_{photoexcited}(\mathbf{r}, t)|^2 \, d\mathbf{r} \\ &= \sum_{k,j} c_k^*(t) c_j(t) \int_{donor} \tilde{\varphi}_k^*(\mathbf{r}, \mathbf{R}(t)) \tilde{\varphi}_j(\mathbf{r}, \mathbf{R}(t)) \, d\mathbf{r} \end{aligned} \quad (7)$$

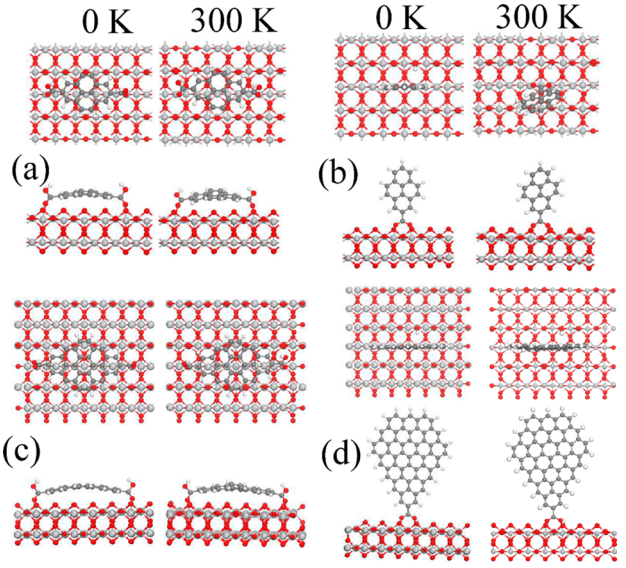

Figure 2. Top and side views of (a) F-pyrene/$Ti_{48}O_{96}$(110), (b) V-pyrene/$Ti_{48}O_{96}$(110), (c) F-coronene/$Ti_{84}O_{168}$(110), and (d) 62-C atom VGQD/$Ti_{84}O_{168}$(110), optimized at 0 K (first and third columns) and during molecular dynamics run at 300 K (second and fourth columns).

The time derivative of eq 7 leads to expressions for the adiabatic and NA contributions to ET:

$$\frac{d \int_{donor} \rho_{photoexcited}(\mathbf{r}, t) \, d\mathbf{r}}{dt} = \sum_{k,j} \left\{ \frac{d(c_i^* c_j)}{dt} \int_{donor} \phi_i^* \phi_j \, d\mathbf{r} + c_i^* c_j \frac{d \int_{donor} \phi_i^* \phi_j \, d\mathbf{r}}{dt} \right\} \quad (8)$$

The first term has fixed localizations of adiabatic states but changing the expansion coefficients, $c_i^* c_j$, which define state occupations if $i = j$. The second term has fixed adiabatic state occupations but changing localizations, $\int_{donor} \phi_i^* \phi_j \, d\mathbf{r}$. The first and second terms correspond to NA ET and adiabatic ET, respectively. The adiabatic ET proceeds by a change in localization of the photoexcited state from a sensitizer to the TiO_2 surface, induced by atomic motions. To undergo a NA transfer, the photoexcited electron has to hop into a TiO_2 state, leading to a change in the state occupations.

Electron injection from the donor molecules and GQD into the TiO_2 surface can occur by three different mechanisms,[37,38,61−65] Figure 1. Namely, the transfer can be adiabatic or NA. Alternatively, it can occur during photoexcitation, such that absorption of a photon generates a charge-separated state directly. The injection is adiabatic in the strong donor−

DOI: 10.1021/jacs.6b09598
J. Am. Chem. Soc. 2017, 139, 2619−2629

acceptor coupling limit. A fluctuation in the atomic coordinates takes the system to a transition state along a reaction coordinate. The system remains continuously in the same electronic state (eigenstate of the electronic Hamiltonian for current atomic coordinates), and the electron density shifts from donor (thick parabola) to acceptor (thin parabola) as the system passes through the transition state (red arrow). The adiabatic ET rate is given by the product of the probability of reaching the transition state and the velocity (inverse frequency) along the reaction coordinate. If the donor−acceptor coupling is weak, the electron remains on the donor (thick parabola) when passing through the transition state. The ET occurs by a NA transition between adiabatic states localized on the donor and acceptor (blue arrow), Figure 1. In the weak coupling limit, the ET rate can be derived using time-dependent perturbation theory, resulting, to the lowest order in the coupling strength, in Fermi's golden rule. In the adiabatic representation, which is available naturally from ab initio electronic structure calculations, the ET happens by transitions (hops) between adiabatic states. The hops are facilitated by NA coupling, hence the NA mechanism. The Fermi golden rule rate is proportional to the product of the coupling squared and the density of acceptor states. Finally, optical selection rules can allow ET to occur already during the photoexcitation process, leading to a (partially) charge separated excited state. A strong donor−acceptor coupling is typically required in this case. Figure 1 denotes the ET photoexcitation process as the direct mechanism. The three mechanisms exhibit different dependences on excitation energy, donor−acceptor bridge/coupling, density of states, and other properties. Therefore, knowledge of the ET mechanism is required for system design.

Diabatic ET is often used in the literature synonymously to NA ET, to describe quantum hops from the donor to the acceptor state. Since the most commonly used ET theory, the Marcus theory, is constructed in the diabatic picture,[62,63,66,67] one considers hops between diabatic rather than adiabatic states. Adiabatic ET that occurs at a transition state, at which one diabatic curve smoothly transforms into the other diabatic curve, forms a single adiabatic state. If a hop between adiabatic states happens at the transition state, no net ET is created, because the hop counteracts the adiabatic ET. The NA ET becomes effective away from the transition state, where the adiabatic and diabatic curves coincide. Therefore, either diabatic or adiabatic states can be used to describe NA ET and to regard it as a quantum hop from one adiabatic (or diabatic) curve to another. While phenomenological models use the diabatic representation because it has a clear physical meaning, ab initio simulations use adiabatic states because they are uniquely defined, in contrast to diabatic states,[62,63,66,67] and are efficiently obtained as eigenstates of the electronic Hamiltonian.

2.3. Autocorrelation Function and Fourier Transform. The fluctuations in the electronic excitation energy, ΔE, caused by atomic motions are characterized by the energy autocorrelation function (ACF)

$$C(t) = \langle \Delta E(t) \Delta E(0) \rangle_T \tag{9}$$

The brackets indicate averaging over a canonical ensemble. The ACF is usually normalized

$$C_{\text{norm}}(t) = \frac{\langle \Delta E(t) \Delta E(0) \rangle_T}{\langle \Delta E^2(0) \rangle_T} \tag{10}$$

by its initial value $C(0) = \langle \Delta E^2(0)_T \rangle$. The square root of this value gives the average fluctuation of the excitation energy.

Fourier transform of an ACF produces the spectral density, also known as the influence spectrum,

$$I(\omega) = \left| \frac{1}{\sqrt{2\pi}} \int_{-\infty}^{\infty} \mathrm{d}t e^{-i\omega t} C(t) \right|^2 \tag{11}$$

which characterizes the vibrational modes involved in the ET process.

The ACF and FT of state localization on the donor, eq 7, characterize the electron−phonon coupling further, emphasizing the modes that couple to the electron density instead of the energy.

2.4. Simulation Details. Geometry optimization, electronic structure, and adiabatic MD simulations were carried out using the Vienna ab initio simulation package.[68,69] Nonlocal exchange-correlation interactions were treated with the Perdew−Burke−Ernzerhof (PBE) DFT functional[70] developed on the basis of the generalized gradient approximation. The semilocal PBE functional is widely accepted as one of the best parameter-free density functionals satisfying the key physical and mathematical requirements of DFT. In particular, PBE obeys the Lieb−Oxford bound,[71] provides the correct linear response of the uniform electron gas with proper uniform scaling,[72] and leads to smooth pseudopotentials.[70] Interactions between ionic cores and valence electrons were described by the projector-augmented wave (PAW) method.[73,74] The DFT +U approach was adopted to describe the local properties of Ti 3d electrons with the on-site U = 6.0 eV and J = 0.5 eV.[37,75] After relaxing the geometry at 0 K, uniform velocity rescaling was used to bring the temperature of the pyrene/TiO_2, coronene/TiO_2, and GQD/TiO_2 systems to 300 K. Then, a 3 ps adiabatic MD simulation for the pyrene/TiO_2 system and a 0.5 ps adiabatic MD simulation for the much larger coronene/TiO_2 and VGQD/TiO_2 systems were carried out in the microcanonical ensemble with a 1 fs atomic time step. The photoexcited electron density was propagated by solving eq 5 using the second-order differencing scheme and a 10^{-3} fs time step. The electronic propagation time step is 1000 times smaller than the nuclear time step, because electrons are significantly lighter than atoms and move faster. The average behavior of the photoinduced ET from pyrene into the TiO_2 surface was obtained using FSSH-NAMD simulations by sampling 500 initial conditions from the adiabatic MD trajectory. The coronene and GQD data were averaged over 100 initial conditions. The length of the trajectory used to sample the initial conditions was chosen in order to represent properly the distribution of the classical phase space variables for the motions that are responsible for the simulated charge transfer. Our analysis shows that the charge transfer dynamics is driven primarily by vibrational modes with frequencies 500 cm^{-1} and above. One ps corresponds to the period of a 33 cm^{-1} mode. Therefore, the chosen 3 and 0.5 ps trajectories provide good sampling (tens of vibrational periods) of the key nuclear motions.

The stoichiometric rutile (110) surface was modeled with a periodically repeated slab containing either a 144-atom surface in the case of pyrene or a 252-atom surface in the case of coronene and GQD, composed of six atomic layers of TiO_2 with the bottom three layers frozen in the bulk configuration, Figure 2. Three electron donors were studied, including the pyrene molecule, $C_{16}H_{10}$, the coronene molecule, $C_{30}H_{14}$, and a

DOI: 10.1021/jacs.6b09598
J. Am. Chem. Soc. 2017, 139, 2619−2629

GQD, $C_{62}H_{20}$, with the edges terminated by hydrogens. The donors were linked to the TiO_2 surface via carboxylic groups −COOH. Each group displaced a hydrogen atom, which was placed next to a bridging oxygen atom on the TiO_2 surface. Flat (F) and vertical (V) arrangements were considered for constructing small combined systems, such as F-pyrene/TiO_2 and V-pyrene/TiO_2, Figure 2. Both arrangements can be achieved experimentally with molecules, GQDs, and other two-dimensional materials, such as MoS_2.[76] Note that placing the $C_{62}H_{20}$ GQD flat on the TiO_2 surface requires a very large simulation cell, extending beyond the computational resources available for the NAMD calculations. Therefore, we consider the GQD in the vertical arrangement only, bound to the $Ti_{84}O_{168}$(110) slab, Figure 2d. Coronene was bound to the same slab in the flat configuration, Figure 2c. Pyrene was bound to a smaller slab in both flat and vertical orientations, Figure 2a,b.

The V-pyrene and VGQD were bound to the TiO_2 surface through a single carboxylic acid group in a bidentate binding geometry, providing two chemical bonds from carboxylic oxygens to the same Ti atom. F-Pyrene and F-coronene were connected to the TiO_2 surface through two carboxylic groups in a monodentate manner, also providing two covalent chemical bonds between the molecular donors and TiO_2 acceptor. The systems were separated from their periodic images along the surface normal by a vacuum region of 15 Å. In order to ensure that the number of NA trajectories used is sufficient to establish the ET mechanism and time scale, we checked convergence with increasing number of trajectories. The initially photoexcited states were chosen by computing the oscillator strength for photon absorption that promotes electrons from the chromophore highest occupied molecular orbital (HOMO) to unoccupied orbitals, and selecting transitions with the largest oscillator strength within the studied energy range. This type of calculation capability has been added to the standard VASP distribution by our group. We have shown previously that this approach for selecting the initially photoexcited state leads to good agreement with experimental data on interfaces of TiO_2 with molecules[28,30] and quantum dots.[33,38] The results obtained for $C_{16}H_{10}$ and $C_{30}H_{14}$ in the flat configuration as well as $C_{16}H_{10}$ and $C_{62}H_{20}$ in the vertical configuration were very similar, both matching the experimental data and indicating that the pyrene molecule already gives a reasonable representation for mimicking the experimental observations of electron injection from GQDs into TiO_2.[18] The minor differences between $C_{16}H_{10}$, $C_{30}H_{14}$, and $C_{62}H_{20}$ are discussed explicitly below.

3. RESULTS AND DISCUSSION

The time scales and mechanisms of the photoinduced electron injection from pyrene, coronene, and GQDs into TiO_2 depend on a number of factors, including the geometric and electronic structure of the interface, and electron−phonon interactions. These factors are analyzed below one at a time, prior to considering the ET process. The charge injection competes with energy relaxation. The interplay between injection and relaxation is discussed at the end.

3.1. Geometric Structure. The binding and relative orientation of electron donors and the TiO_2 surface determine the physical and chemical interactions between the electron donor and acceptor. The geometric structure also influences the vibrational modes that couple to the electronic subsystem. Therefore, knowledge of the system geometry constitutes the first step in the analysis of the ET mechanism and time scale, as well as the competition between ET and energy relaxation. Since thermal fluctuations at room temperature may affect the structure, we consider both the geometries optimized at 0 K and representative geometry snapshots from the room temperature MD trajectories, Figure 2. The geometries of the flat systems change little upon heating, because they are connected to the TiO_2 surface at the two ends. A flat GQD that is not chemically bound to TiO_2 can slide along the surface. The vertical systems undergo large-scale bending motions with respect to the surface. They cannot lie flat, because the carboxylic acid linker group is short. The carboxylic group provides strong binding.

Considering the F-pyrene/TiO_2 system, Figure 2a, we observe that pyrene maintains two bonds to the TiO_2 substrate at both 0 K and room temperature. The situation remains unchanged in the F-coronene/TiO_2 system, Figure 2c. The optimized structure of F-pyrene/TiO_2 is slightly asymmetric: the O−Ti bond lengths are 2.292 and 2.232 Å. The bonds oscillate at finite temperatures. To characterize the room temperature binding geometry, we compute canonically averaged bond lengths. The average length of the left O−Ti bond in F-pyrene/TiO_2 decreases from 2.292 Å at 0 K to 2.278 Å at room temperature, while the right bond elongates from 2.232 to 2.312 Å. One side of pyrene inclines toward the TiO_2 surface, decreasing the pyrene/TiO_2 separation, and hence increasing the donor−acceptor interaction through the π-electron system. The corresponding bond angles fluctuate as well. It is important for the adiabatic ET mechanism that the strong interaction between the donor and acceptor materials is maintained or enhanced at room temperature.

In the V-pyrene/TiO_2 system, Figure 2b, pyrene is connected to TiO_2 via two carboxylic O atoms binding to the same Ti. The geometry of V-GQD/TiO_2 is shown in Figure 2d. The structures are slightly asymmetric. The bond lengths in Figure 2b are 2.086 and 2.110 Å at 0 K. As temperature increases to ambient conditions, both bonds shorten on average. The O−Ti bond lengths averaged at room temperature are 2.061 and 2.104 Å, respectively. Counter to intuition, the donor−acceptor distance becomes shorter at an elevated temperature. This is because thermal fluctuations disrupt the fully optimized structure of the TiO_2 surface, creating additional bonding opportunities. The root-mean-squared deviations (RMSDs) for the two O−Ti bonds are very similar: 0.0747 vs 0.0745 Å. In comparison, the RMSD values in the F-pyrene/TiO_2 system differ. They are 0.116 and 0.163 Å for the left and right O−Ti bonds, respectively. The RMSDs are larger for F-pyrene than the V-pyrene, indicating that thermal fluctuations have a more pronounced effect on coupling in the F-pyrene/TiO_2 system. In both systems, the distributions of the bond lengths obtained from the 3 ps trajectories are close to Gaussian, as should be expected for the relatively harmonic O−Ti bond vibrations.

The binding energies are 2.335 and 2.668 eV for the F-pyrene/TiO_2 and V-pyrene/TiO_2 systems shown in Figure 2a and b. The values include the van der Waals interaction implemented by the DFT-D2 method of Grimme.[77] The binding energies are similar, with V-pyrene exhibiting a 10−15% stronger binding. Remarkably, by turning the van der Waals interaction off, we obtain vastly different binding energies: 0.995 eV for F-pyrene/TiO_2 and 2.102 eV for V-pyrene/TiO_2. The difference reveals two important facts. First, the van der Waals interaction in the F-pyrene system is responsible for 60% of the pyrene/TiO_2 binding energy.

DOI: 10.1021/jacs.6b09598
J. Am. Chem. Soc. 2017, 139, 2619−2629

Second, excluding the van der Waals interaction reveals that the two covalent bonds of the carboxylic acid linkers are twice weaker for F-pyrene than V-pyrene. Thus, we conclude that the pyrene/TiO_2 covalent bonding is much stronger for V-pyrene than F-pyrene, and that F-pyrene is bound to TiO_2 primarily via the van der Waals attraction facilitated by the π-electron system.

Bending of V-pyrene toward TiO_2, the surface is energetically unfavorable in the absence of the second linker group. Thus, the V-pyrene/TiO_2 binding energy changes from 2.668 eV for the vertical geometry (0° tilt), to 2.411 eV for the 45° tilt, to 2.126 eV for the 60° tilt. V-Pyrene is bound to TiO_2 through a single carboxylic group in a bidentate manner. In comparison, F-pyrene is bound to TiO_2 through two carboxylic groups in a monodentate manner for each group. Disconnecting one of the groups and changing the tilt angle from 90° (flat pyrene) to 60 and 45° changes the binding energy from 2.335 to 1.103 and 1.120 eV, respectively. Compared to the bidentate binding, bending pyrene bound to TiO_2 in a monodentate manner involves a much smaller penalty, as reflected by the small decrease of the binding energy from 1.120 to 1.103 eV upon bending from 45 to 60° relative to the surface normal. The second carboxylic group doubles the binding energy, counteracting the bending penalty and making the F-pyrene/TiO_2 system energetically stable.

3.2. Electronic Structure. Figure 3 show the electron densities of the donor and acceptor states at room temperature.

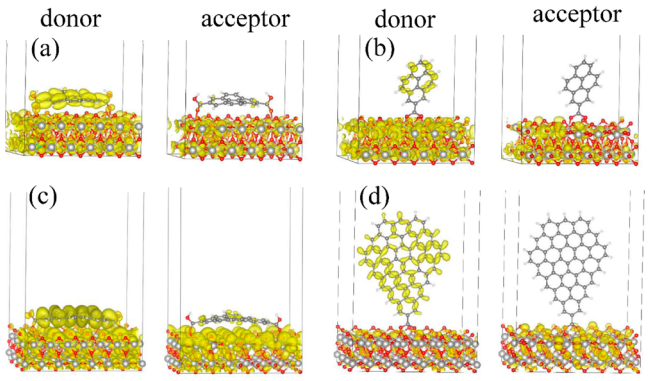

Figure 3. Charge densities of photoexcited donor states (left panel) and acceptor states (right panel) in (a) F-pyrene/TiO_2, and (b) V-pyrene/TiO_2, (c) F-coronene/TiO_2, and (d) VGQD/TiO_2. The photoexcited states are delocalized between donor and acceptor, while the acceptor states are localized in TiO_2. The covalent bonding combined with π-electron interaction in the F-pyrene/TiO_2 and F-coronene/TiO_2 systems provides multiple strong coupling channels. The photoexcited state in V-pyrene is localized away from TiO_2, and the donor–acceptor coupling is weak. More than half of the electron state density is localized on the GQD in the VGQD/TiO_2 system. There is no electron density on the carboxylic bridge connecting the GQD to TiO_2, resulting in weak donor–acceptor coupling. The strong donor–acceptor coupling leads to adiabatic ET in both F-pyrene/TiO_2 and F-coronene/TiO_2. The weak donor–acceptor coupling leads to NA ET in V-pyrene/TiO_2 and VGQD/TiO_2, Figure 1.

The density of the photoexcited electron in the F-pyrene/TiO_2 system is spread uniformly across the pyrene, and is delocalized between pyrene and the TiO_2 slab (left panel of Figure 3a). The acceptor state is spread across the TiO_2 slab, with a tail extending onto the pyrene (right panel of Figure 3a). The electronic interaction between F-pyrene and TiO_2 proceeds primarily through noncovalent coupling of the π-electron subsystem of F-pyrene with the 3d-electrons of the undercoordinated Ti atoms of the semiconductor surface. This fact is supported by the larger contribution of the van der Waals interaction to the binding energy, compared to the covalent bonding; see the previous section. The observations agree with the first-principles calculations, including the dispersion correction, carried out by Liu on the TiO_2(101) surface interfaced with infinite graphene and graphdiyne.[78] The calculations demonstrated that the interaction between graphene and the TiO_2(101) surface is pure van der Waals. However, the interaction between graphdiyne and TiO_2(101) occurs at 0 K through C–O covalent bonds due to wrinkling of the graphdiyne sheet, which facilitates charge transfer.[78] The situation is similar to the graphene/TiO_2(110) interface. As temperature increases to ambient conditions, the interaction at the graphene/TiO_2(110) surface attains covalent character that is beneficial for ET.[37]

The photoexcited state of V-pyrene has no density on the carboxylic acid bridge connecting it to the TiO_2 surface (left panel of Figure 3b). Even though the covalent bonding between the donor and acceptor is strong, the π-electron withdrawing properties of the carboxylic group breaks the electronic coupling. The situation is different from a number of other studied systems, including organic molecules[28] and inorganic QDs[33] covalently bound to TiO_2. The key role played by the through-space interaction in the F-pyrene/TiO_2 system is similar to that observed for TiO_2/graphene[37] and TiO_2/water.[39] The density of the acceptor state in V-pyrene/TiO_2 is confined entirely within the TiO_2 slab (right panel of Figure 3b). The photoexcited electron donor and acceptor states of the larger F-coronene/TiO_2 system (Figure 3c) and VGQD/TiO_2 (Figure 3d) show charge localization that is similar to F-pyrene/TiO_2 and V-pyrene/TiO_2. The strong donor–acceptor coupling in F-pyrene/TiO_2 and F-coronene/TiO_2 leads to the adiabatic ET mechanism. The absence of the photoexcited electron density at the carboxylic linker leads to weak donor–acceptor coupling and NA ET in the V-pyrene/TiO_2 and VGQD/TiO_2 systems. Vertically aligned pyrene and GQD can undergo large-scale tilting with respect to the TiO_2 surface. Sampling such motion requires significantly larger simulation cells and longer trajectories. More importantly, the current study emphasizes dependence of the ET mechanism on vertical vs horizontal arrangements of the donor and acceptor species. A tilting motion would constitute an intermediate situation between the two limits under investigation, and therefore, one can expect that the charge transfer process in a tilted system will exhibit intermediate features.

In all cases, the photoexcited state is delocalized significantly onto the TiO_2 surface, indicating that absorption of a photon already gives a partially charge-separated state. As the size of the flat donor increases, compare left panels of Figure 3a and c, the photoexcited electron remains shared by the donor and TiO_2, and the adiabatic ET mechanism remains dominant compared to NA ET. Comparing the vertical systems, left panels of Figure 3b with d, a larger fraction of the photoexcited electron remains confined within the chromophore, as the chromophore becomes bigger, and the role of the direct ET mechanism decreases, Figure 1. One can expect that, for the larger GQDs used in the experiment,[18] the NA mechanism fully dominates for the vertical orientation, while a combination of adiabatic and direct ET mechanisms function for the flat orientation.

Our DFT calculations show an energy gap of 2.7 eV between pyrene HOMO and LUMO, Figure S1. This value is

DOI: 10.1021/jacs.6b09598
J. Am. Chem. Soc. 2017, 139, 2619–2629

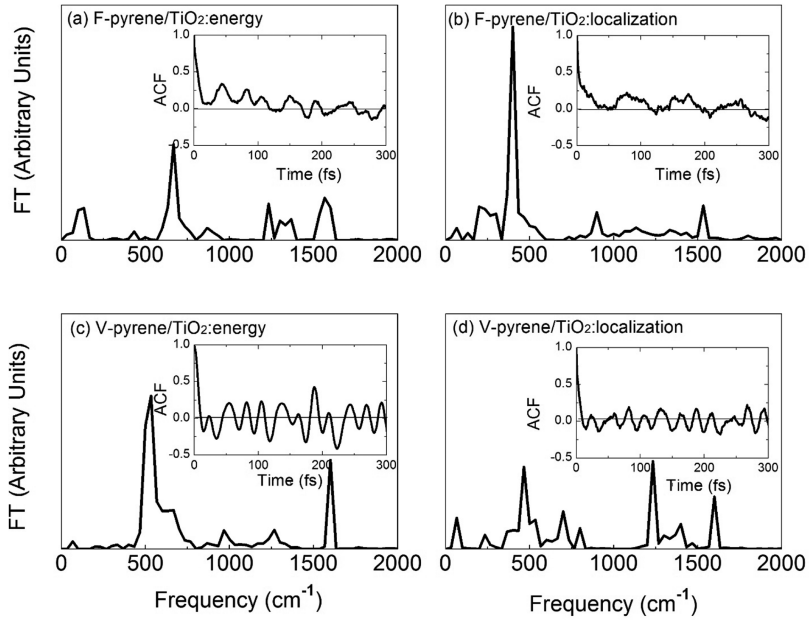

Figure 4. Phonon modes involved in the photoinduced ET processes in (a, b) F-pyrene/TiO_2 and (c, d) V-pyrene/TiO_2. The spectra are obtained by computing Fourier transforms of the autocorrelation functions (insets) of the fluctuations of (a, c) energy and (b, d) localization of the photoexcited states.

underestimated[79] by 0.65 eV relative to the experimental excitation energy of pyrene, due to the well-known self-interaction problem of GGA functionals, including PBE used here. The hybrid B3LYP functional overestimates the HOMO−LUMO gap by 0.53 eV. Addition of carboxylic acid groups slightly decreases the energy gap. The HOMO−LUMO transition is the lowest energy optically active excitation for both pyrene and pyrene decorated with carboxylic acid group(s). Binding to TiO_2 modifies the HOMO−LUMO gap further, and broadens the LUMO.[79] The lowest energy excitation in the pyrene/TiO_2 systems is a charge transfer state, in which the electron moves from the pyrene HOMO to the TiO_2 conduction band minimum (CBM), Figure S1. This 1.8 eV excitation does not exhibit strong optical activity.[79]

3.3. Electron−Phonon Interactions. Vibrational motions of the atoms drive the ET dynamics. They induce fluctuations of the photoexcited state energy and localization, taking the system to the transition state during adiabatic ET. They also create the NA coupling, promoting NA ET. At the same time, electron-vibrational energy exchange causes relaxation and losses of electronic energy to heat. Energy relaxation competes with ET, and a rapid relaxation can prevent ET from happening altogether. Not all vibrational modes available in a particular material couple to the electronic subsystem. In order to characterize the active modes, we compute FTs of the ACFs of the photoexcited state energy and localization in the F-pyrene/TiO_2 and V-pyrene/TiO_2 systems, Figure 4. The result is known as the influence spectrum, or spectral density, eq 11. The electrons couple to a broad spectrum of vibrations with frequencies ranging from under 100 cm^{-1}, corresponding to slow large-scale motions, to 1600 cm^{-1} C−C stretching vibrations. Because the pyrene molecule is less rigid than TiO_2, and has lighter and faster moving atoms, pyrene vibrations are more important for the ET dynamics than TiO_2 phonons. Generally, the wave function localization couples to a broader range of vibrational motions than the energy. The ACF recurrences (secondary peaks at later times) are less pronounced for F-pyrene than V-pyrene, because the F-pyrene system couples to more modes. F-Pyrene is more closely coupled to the TiO_2 substrate than V-pyrene, and therefore, TiO_2 vibrations contribute more strongly to the former case. Note that the differences in the ET mechanisms for the two conformations arise from differences in the donor−acceptor interactions rather than electron−phonon coupling.

The strongest electron−phonon coupling is observed for the modes around 500 cm^{-1}, with a period of about 60 fs. The second highest coupling is for the modes around 1500 cm^{-1}, with a period of about 20 fs. The fact that the ET happens on a sub-15 fs time scale indicates that only a fraction of the period of the key modes is required. This observation can be rationalized by the presence of multiple acceptor states. The electron is transferred into the TiO_2 conduction band, and many TiO_2 states exist that couple to the electron donor. In the case of the adiabatic mechanism, only a fraction of the vibrational period is needed to change the relative energies of the donor and multiple acceptor states, in order to bring the system toward one of many transition states. In the case of the NA mechanism, quantum transitions from the initial to multiple final states are possible. The fact that many phonon modes generate the electron−phonon coupling indicates that there are multiple reaction coordinates for the adiabatic transfer, and that one can always find several active modes with large velocities to generate the NA coupling.

Focusing on particular vibrational frequencies seen in the FT spectra of the photoexcited energy and localization, we can identify a number of peaks in the 500−2000 cm^{-1} regions. The 1540 cm^{-1} peak is a fingerprint of the graphene G-band,[80] arising from C−C stretching. The peak at 1380 cm^{-1} corresponds to the D-band, stemming from the breathing modes of sp^2 hybridized carbon rings.[80,81] The peaks between 500 and 700 cm^{-1} can be seen in the rutile TiO_2 Raman spectrum.[82] The peak at 800 cm^{-1} is associated with the high-frequency polar longitudinal optical phonons of TiO_2.[83] These vibrations change dipole moments of the polar Ti−O bonds,

DOI: 10.1021/jacs.6b09598
J. Am. Chem. Soc. 2017, 139, 2619−2629

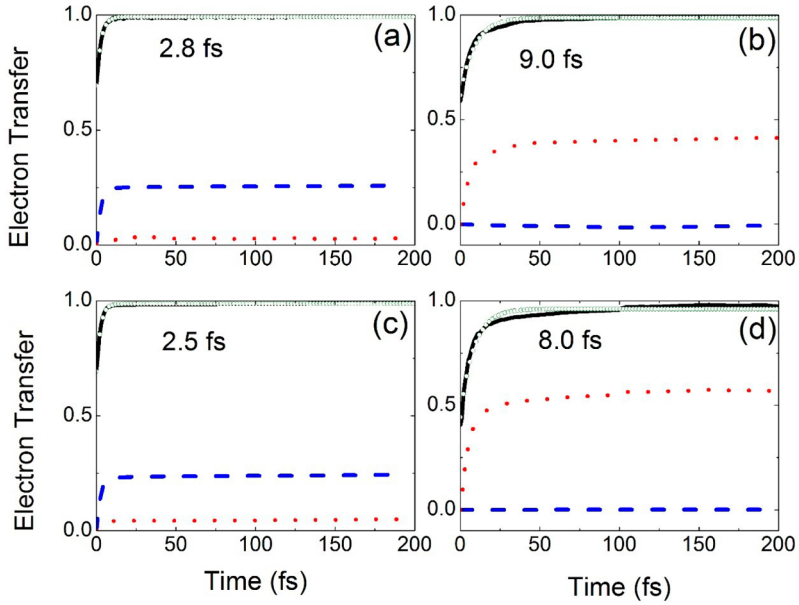

Figure 5. ET from (a) F-pyrene, (b) V-pyrene, (c) F-coronene, and (d) VGQD into TiO_2. The solid black, dashed blue, and dotted red lines represent the total, adiabatic, and NA ET, respectively. In both pyrene and coronene sensitized TiO_2, a significant fraction of electron density is transferred to TiO_2 already during photoexcitation, corresponding to direct ET that is characterized by the *y*-axis intercept of the total ET curve. In the VGQD/TiO_2 system, less than half of the photoexcited electron density is localized on TiO_2 after the excitation. Subsequently, the adiabatic mechanism dominates ET for the flat systems, while the NA mechanism governs ET in vertical systems. The circles show exponential fits of the total ET data.

and therefore, they couple to the electronic degrees of freedom. The TiO_2 vibrational modes take part in the calculated FT spectra because the photoexcited state delocalizes onto TiO_2, Figure 3a and b.

3.4. Electron Injection. The time scales of the photo-induced ET from the pyrene, coronene, and GQD into the TiO_2 substrate are under 15 fs, Figure 5, in excellent agreement with the experimental data.[18] The transfer is faster for F-pyrene, 2.8 fs, than V-pyrene, 9.0 fs, Figure 5a and b. Increase of the donor size from pyrene to coronene and GQD has little effect on the injection time, Figure 5c and d. 2.8 fs changes to 2.5 fs, and 9.0 fs changes to 8.0 fs. The injections from the flat systems are faster than those from the vertical systems, because the donor–acceptor coupling is stronger. The total electron transfer curves start at values significantly above 0, because the photoexcited states are delocalized onto the TiO_2 acceptor. Note that ET from graphene adsorbed on bulk TiO_2 is significantly slower than that from the finite systems studied here.[19,37] One expects a momentum barrier to the ET in the case of graphene,[18] since the electrons are excited near the K-point in the momentum space in graphene, while the CBM of the TiO_2 acceptor is at the Γ-point. Therefore, the graphene/TiO_2 ET is accompanied by phonon scattering accommodating the momentum change. In contrast, the photoexcited electron does not have a well-defined momentum in a finite system, and the momentum barrier to the ET does not exist.

The total, adiabatic, and NA ET components are presented in Figure 5 by the black solid, blue dashed, and red dotted lines, respectively. The total ET data were fitted by the exponential function $f(t) = f(t_0) + A[1 - \exp(-t/\tau)]$, where τ is the ET time constant and A denotes the sum of the amplitudes of the adiabatic and NA contributions to the overall ET. The $f(t_0)$ term represents the contribution of the direct ET mechanism, which is characterized by the *y*-axis intercept. The through-bond donor–acceptor coupling in the vertically aligned systems is weak due to π-electron withdrawing properties of the carboxylic acid linker, which contains no electron density, left panels of Figure 3b and d. As a result, the ET is NA. In comparison, the through-space donor–acceptor interaction provided by the π-electron system of F-pyrene and F-coronene is strong, resulting in adiabatic ET. One expects an opposite behavior a priori. For instance, π-electron stacking interactions between different chains in conjugated polymers[84,85] or DNA nucleotides[86] induce electron hops, i.e., NA ET, while ET in many covalently bound donor–acceptor systems is adiabatic.[87,88]

The through-bond interaction by the linker group provides weaker donor/acceptor coupling than the through-space interaction via the conjugated π-electron system. This key and counterintuitive conclusion obtained for the current systems should only become stronger for larger GQDs. With increasing system size, the π-electron system grows, while the linker between the donor and acceptor subsystems remains the same. Therefore, the contribution of the through-bond interaction remains the same, while the contribution of the π-electron system increases. If the through-bond interaction is weaker than the through-space interaction already for pyrene, as well as for coronene and the GQD considered here, it should be even weaker as the size of the π-system increases.

The vertically aligned donor species can undergo large-scale tilting with respect to the TiO_2 surface. Sampling this motion would require significantly larger simulation cells and long trajectories. More importantly, the current study emphasizes the differences between the vertical and horizontal arrangements. A tilting motion would constitute an intermediate situation between the two considered limits, and therefore, one can expect that the charge transfer features will also be intermediate between the two established mechanisms.

The linker between the electron donors and TiO_2 surface affects the localization of the donor wave function, the overlap

DOI: 10.1021/jacs.6b09598
J. Am. Chem. Soc. 2017, 139, 2619–2629

of the donor and acceptor states, and the NA coupling. Our study shows that the electron withdrawing carboxylic acid group breaks the donor−acceptor conjugation. One can expect that an electron donating linker would have the opposite effect and increase the donor−acceptor coupling. Then, the ET in the vertically aligned systems could occur by the adiabatic mechanism.

Persson and co-workers[79] investigated systemically the interaction between TiO_2 nanoparticles and pyrene with various spacers and anchor groups using DFT and TD-DFT calculations employing the hybrid B3LYP functional, and discussed the electronic structure and excited state properties.[89] The calculations showed that the interaction between the molecular electron donor and TiO_2 acceptor can be tuned by changing the spacer lengths, anchor groups, and binding positions. Persson and co-workers have shown that appropriate modifications of the pyrene molecule can enhance long-range electronic interactions across the interface, shift charge densities closer to the TiO_2 surface, and facilitate charge separation for solar cell applications.[79]

3.5. Energy Relaxation. In an efficient photovoltaic cell, charge separation should be faster than electron−phonon energy relaxation. Figure 6 characterizes the relaxation process

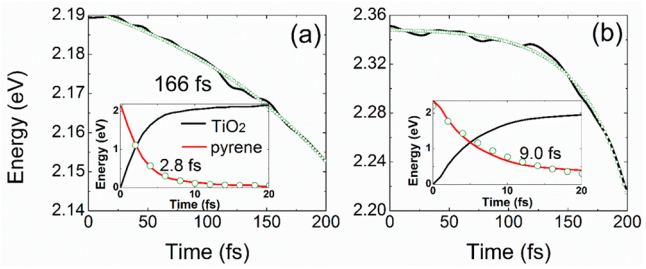

Figure 6. Phonon-induced relaxation of electronic energy during electron injection in (a) F-pyrene/TiO_2 and (b) V-pyrene/TiO_2. In both cases, the energy relaxation is slower than the ET, Figure 5a and b, indicating that efficient charge separation can be obtained. The insets illustrate transfer of electron energy from pyrene (red line) to TiO_2 (black line). The energy transfer is faster than the overall energy relaxation, as evidenced by transient heating of TiO_2.

of the F-pyrene/TiO_2 and V-pyrene/TiO_2 systems. The main plots depict losses of the overall electronic energy to vibrations on a longer time scale. The insets show the evolution of the electronic energy within the donor and acceptor subsystems on a time scale comparable with the ET times. The data shown in Figure 6a are fitted by the exponential function $f(t) = f(t_0) + B\exp(-t/\tau)$. In the current fit, τ is the energy relaxation time constant, $f(t_0)$ represents the initial energy, and the amplitude B is determined by the energy range included in the calculation. Note that the total energy relaxation curve for the V-pyrene/TiO_2 (cf. Figure 6b) cannot be fitted to a single exponent. In general, quantum dynamics at early times involves relatively few states that are directly coupled to the initial state. Such dynamics are slow, corresponding to the beginning of a Rabi oscillation (or Gaussian decay), with zero first derivative at time 0. As the dynamics involve more and more states at later times, via higher order couplings to the initial state, the relaxation accelerates and becomes exponential, as described, for instance, by the Fermi golden rule.

Our simulations show that the energy relaxation is an order of magnitude slower than the charge separation for both F-pyrene and V-pyrene. This is a necessary condition for photovoltaic and photocatalytic applications of GQD/TiO_2 composites. Interestingly, the calculated energy relaxation times are at least 2 orders of magnitude smaller than those of isolated GQDs, according to both experiment[17] and theory.[20] There is no inconsistency here. The relaxation is fast in the current simulation due to participation of TiO_2. Similar to pyrene molecules, GQDs have discrete energy levels, while TiO_2 has a continuous density of states in the conduction band. Note that the short-time components of the total energy relaxation curves are flat, Figure 6. The relaxation accelerates dramatically after the electron is transferred into TiO_2, and the conduction band continuum becomes accessible.

The ET transfer is faster than the energy relaxation in the graphene/TiO_2 composite as well.[37] The difference in the charge separation and relaxation times is more critical for graphene, because it has a continuous energy spectrum, similarly to TiO_2, though the density of states is lower for graphene than the TiO_2 surface due to thickness differences. Electron−phonon energy exchange is much faster in graphene[90] than in GQDs.[17,20] Therefore, it is essential that the photogenerated electron is removed from graphene on an ultrafast time scale.[19] It is not a problem in current systems, because molecules and GQDs have a wide energy gap that ensures long-lived photoexcited electrons. It is interesting to note that, even though the donor−acceptor interaction proceeds via the π-electron system in both graphene/TiO_2 and the finite systems in the flat orientation studied here, the ET mechanisms are different. The ET is NA and relatively slow in the case of graphene, while the ET is adiabatic and fast for the finite systems. The difference arises because the linkers bring the π-orbitals of the finite system closer to the TiO_2 surface, enhancing the donor−acceptor interaction. For example, the average graphene/TiO_2 distance is 2.617 Å for the optimized geometry, while the average distance in F-pyrene/TiO_2 is 2.435 Å at 0 K.

The insets in Figure 6 characterize electronic energy transfer from the pyrene molecules into TiO_2. The plots are obtained by combining the data for ET and total energy relaxation. The insets separate the total excess energy into contributions stemming from pyrene and TiO_2. Because the ET is faster than the electronic energy relaxation, the TiO_2 surface heats up initially. In each case, the energy transfer proceeds simultaneously with the ET and is significantly faster than the energy relaxation. Note the identical time scales obtained from the fits of the excess energy, Figure 6 insets, and the total ET, Figure 5.

4. CONCLUSIONS

In summary, we have characterized the chemical, geometric, and electronic structure of pyrene/TiO_2, coronene/TiO_2, and GQD/TiO_2 composites, and established the mechanisms and time scales of the photoinduced interfacial electron and energy transfer, and energy relaxation. The study has been performed at the ab initio atomistic level and explicitly in time, mimicking directly the pump−probe experimental data. A mixed quantum-classical approach combining real-time time-dependent density functional theory with nonadiabatic molecular dynamics has been used.

The simulations reveal a strong and, arguably, counter-intuitive dependence of the donor−acceptor coupling and ET mechanism on the type of chemical bonding. We show that covalent bonding produces weak donor−acceptor coupling and gives the nonadiabatic ET mechanism. In contrast, through-

DOI: 10.1021/jacs.6b09598
J. Am. Chem. Soc. 2017, 139, 2619−2629

space interaction of π-electrons of the donor species with the under-coordinated TiO_2 surface atoms creates strong donor−acceptor coupling, resulting in adiabatic ET. A priori knowledge based on other systems, such as donor−acceptor molecular diads and triads, conjugated polymers, and DNA, leads to the opposite expectation. The findings are rationalized by the π-electron withdrawing properties of the carboxylic acid group linker, and by the notable chemical activity of under-coordinated TiO_2 surface atoms. The key conclusion already obtained with pyrene and supported further by the calculation for the larger systems, namely, that the donor−acceptor interaction through the π-system is more important than the interaction through the linker, becomes even stronger with increasing system size. As the size of the molecule/GQD grows, the size of the π-electron system grows as well, while the linker remains the same. Therefore, the relative contribution of the π-electron system to the donor−acceptor interaction should increase with increasing system size.

The calculated ET times show excellent agreement with the time-resolved experimental data. The calculations show that the photoexcited state has a partial charge transfer character. The electronic subsystem couples to a broad spectrum of vibrational motions during the ET process. The vibrations are primarily those of the donors, which are less rigid than TiO_2 and contain lighter, faster moving atoms. The charge separation is significantly faster than the energy relaxation. This condition is essential for successful application of GQD/TiO_2 composites in photocatalysis and photovoltaics, because it leads to long-lived charge separated states.

The clear demonstration and rationalization of the effect of binding configurations on the mechanism of the photoinduced ET provides important guidelines for the design of high performance solar cells. The conclusions of the present study should apply to other heterojunctions, including interfaces of bulk semiconductors with large molecular chromophores and a variety of linker moieties, with two-dimensional materials, such as graphene and MoS_2, as well as to multicomponent nanoscale systems in general. The established principles allow one to apply chemical tools in order to tune the properties of hybrid nanoscale materials for use in electronic and spintronic devices, solar energy harvesting and utilization, etc.

■ ASSOCIATED CONTENT

Supporting Information

The Supporting Information is available free of charge on the ACS Publications website at DOI: 10.1021/jacs.6b09598.

Projected density of states for the two pyrene/TiO_2 systems, total energies, and optimized atomic coordinates for all systems under investigation (PDF)

■ AUTHOR INFORMATION

Corresponding Authors

*runlong@bnu.edu.cn
*prezhdo@usc.edu

ORCID

Oleg V. Prezhdo: 0000-0002-5140-7500

Notes

The authors declare no competing financial interest.

■ ACKNOWLEDGMENTS

R.L. is grateful to the National Science Foundation of China, Grant No. 21573022, the Recruitment Program of Global Youth Experts of China and Beijing Normal University Startup. W.-H.F. thanks the National Science Foundation of China for support under Grant Nos. 21520102005 and 21421003. D.C. acknowledges support from the Basque Government (project IT588-13) and IKERBASQUE, Basque Foundation for Science. O.V.P. acknowledges support of the U.S. National Science Foundation, Grant No. CHE-1565704, and is grateful to the High-End Foreign Experts Recruitment Program for support during a visit to Beijing Normal University.

■ REFERENCES

(1) Abbas, A. N.; Liu, B. L.; Narita, A.; Dossel, L. F.; Yang, B.; Zhang, W.; Tang, J. S.; Wang, K. L.; Rader, H. J.; Feng, X. L.; Mullen, K.; Zhou, C. W. *J. Am. Chem. Soc.* **2015**, *137*, 4453−4459.
(2) Lu, C.-C.; Lin, Y.-C.; Yeh, C.-H.; Huang, J.-C.; Chiu, P.-W. *ACS Nano* **2012**, *6*, 4469−4474.
(3) Worsley, M. A.; Pauzauskie, P. J.; Olson, T. Y.; Biener, J.; Satcher, J. H.; Baumann, T. F. *J. Am. Chem. Soc.* **2010**, *132*, 14067−14069.
(4) Balandin, A. A.; Ghosh, S.; Bao, W.; Calizo, I.; Teweldebrhan, D.; Miao, F.; Lau, C. N. *Nano Lett.* **2008**, *8*, 902−907.
(5) Bolotin, K. I.; Sikes, K. J.; Jiang, Z.; Klima, M.; Fudenberg, G.; Hone, J.; Kim, P.; Stormer, H. L. *Solid State Commun.* **2008**, *146*, 351−355.
(6) Stoller, M. D.; Park, S.; Zhu, Y.; An, J.; Ruoff, R. S. *Nano Lett.* **2008**, *8*, 3498−3502.
(7) Liu, H.; Ryu, S.; Chen, Z.; Steigerwald, M. L.; Nuckolls, C.; Brus, L. E. *J. Am. Chem. Soc.* **2009**, *131*, 17099−17101.
(8) Xiang, Q.; Yu, J.; Jaroniec, M. *Chem. Soc. Rev.* **2012**, *41*, 782−796.
(9) Zhang, L.; Diao, S.; Nie, Y.; Yan, K.; Liu, N.; Dai, B.; Xie, Q.; Reina, A.; Kong, J.; Liu, Z. *J. Am. Chem. Soc.* **2011**, *133*, 2706−2713.
(10) Li, Q.; Guo, B.; Yu, J.; Ran, J.; Zhang, B.; Yan, H.; Gong, J. R. *J. Am. Chem. Soc.* **2011**, *133*, 10878−10884.
(11) Zhang, Y.; Zhang, N.; Tang, Z.-R.; Xu, Y.-J. *Phys. Chem. Chem. Phys.* **2012**, *14*, 9167−9175.
(12) Xiang, Q.; Yu, J.; Jaroniec, M. *J. Am. Chem. Soc.* **2012**, *134*, 6575−6578.
(13) Loh, K. P.; Tong, S. W.; Wu, J. *J. Am. Chem. Soc.* **2016**, *138*, 1095−1102.
(14) Park, H.; Chang, S.; Smith, M.; Gradecak, S.; Kong, J. *Sci. Rep.* **2013**, *3*, 1581.
(15) Gomez De Arco, L.; Zhang, Y.; Schlenker, C. W.; Ryu, K.; Thompson, M. E.; Zhou, C. *ACS Nano* **2010**, *4*, 2865−2873.
(16) Gupta, V.; Chaudhary, N.; Srivastava, R.; Sharma, G. D.; Bhardwaj, R.; Chand, S. *J. Am. Chem. Soc.* **2011**, *133*, 9960−9963.
(17) Mueller, M. L.; Yan, X.; Dragnea, B.; Li, L.-S. *Nano Lett.* **2011**, *11*, 56−60.
(18) Williams, K. J.; Nelson, C. A.; Yan, X.; Li, L.-S.; Zhu, X. *ACS Nano* **2013**, *7*, 1388−1394.
(19) Manga, K. K.; Zhou, Y.; Yan, Y.; Loh, K. P. *Adv. Funct. Mater.* **2009**, *19*, 3638−3643.
(20) Jaeger, H. M.; Green, J. R.; Prezhdo, O. V. *Appl. Phys. Lett.* **2013**, *103*, 073111.
(21) Georgakilas, V.; Perman, J. A.; Tucek, J.; Zboril, R. *Chem. Rev.* **2015**, *115*, 4744−4822.
(22) Mora-Seró, I.; Giménez, S.; Fabregat-Santiago, F.; Gómez, R.; Shen, Q.; Toyoda, T.; Bisquert, J. *Acc. Chem. Res.* **2009**, *42*, 1848−1857.
(23) Craig, C. F.; Duncan, W. R.; Prezhdo, O. V. *Phys. Rev. Lett.* **2005**, *95*, 163001.
(24) Tully, J. C. *J. Chem. Phys.* **1990**, *93*, 1061−1071.
(25) Fischer, S. A.; Habenicht, B. F.; Madrid, A. B.; Duncan, W. R.; Prezhdo, O. V. *J. Chem. Phys.* **2011**, *134*, 024102−9.
(26) Akimov, A. V.; Prezhdo, O. V. *J. Chem. Theory Comput.* **2014**, *10*, 789−804.

DOI: 10.1021/jacs.6b09598
J. Am. Chem. Soc. 2017, 139, 2619−2629

(27) Akimov, A. V.; Prezhdo, O. V. *Chem. Rev.* **2015**, *115*, 5797−5890.
(28) Duncan, W. R.; Craig, C. F.; Prezhdo, O. V. *J. Am. Chem. Soc.* **2007**, *129*, 8528−8543.
(29) Duncan, W. R.; Prezhdo, O. V. *J. Am. Chem. Soc.* **2008**, *130*, 9756−9762.
(30) Duncan, W. R.; Stier, W. M.; Prezhdo, O. V. *J. Am. Chem. Soc.* **2005**, *127*, 7941−7951.
(31) Stier, W.; Prezhdo, O. V. *Isr. J. Chem.* **2002**, *42*, 213−224.
(32) Duncan, W. R.; Prezhdo, O. V. *J. Phys. Chem. B* **2005**, *109*, 17998−18002.
(33) Long, R.; Prezhdo, O. V. *J. Am. Chem. Soc.* **2011**, *133*, 19240−19249.
(34) Tafen, D. N.; Long, R.; Prezhdo, O. V. *Nano Lett.* **2014**, *14*, 1790−1796.
(35) Long, R.; English, N. J.; Prezhdo, O. V. *J. Phys. Chem. Lett.* **2014**, *5*, 2941−2946.
(36) Tafen, D.; Prezhdo, O. V. *J. Phys. Chem. C* **2015**, *119*, 5639−5647.
(37) Long, R.; English, N. J.; Prezhdo, O. V. *J. Am. Chem. Soc.* **2012**, *134*, 14238−14248.
(38) Long, R.; Prezhdo, O. V. *J. Am. Chem. Soc.* **2014**, *136*, 4343−4354.
(39) Fischer, S. A.; Duncan, W. R.; Prezhdo, O. V. *J. Am. Chem. Soc.* **2009**, *131*, 15483−15491.
(40) Liu, J.; Prezhdo, O. V. *J. Phys. Chem. Lett.* **2015**, *6*, 4463−4469.
(41) Long, R.; Fang, W. H.; Prezhdo, O. V. *J. Phys. Chem. Lett.* **2016**, *7*, 3215−3222.
(42) Long, R.; Liu, J.; Prezhdo, O. V. *J. Am. Chem. Soc.* **2016**, *138* (11), 3884−3890.
(43) Long, R.; Prezhdo, O. V. *ACS Nano* **2015**, *9*, 11143−11155.
(44) Akimov, A. V.; Prezhdo, O. V. *J. Am. Chem. Soc.* **2014**, *136*, 1599−1608.
(45) Kilin, D. S.; Tsemekhman, K.; Prezhdo, O. V.; Zenkevich, E. I.; von Borczyskowski, C. *J. Photochem. Photobiol., A* **2007**, *190*, 342−351.
(46) Zhu, H. M.; Yang, Y.; Hyeon-Deuk, K.; Califano, M.; Song, N. H.; Wang, Y. W.; Zhang, W. Q.; Prezhdo, O. V.; Lian, T. Q. *Nano Lett.* **2014**, *14*, 1263−1269.
(47) Akimov, A. V.; Muckerman, J. T.; Prezhdo, O. V. *J. Am. Chem. Soc.* **2013**, *135*, 8682−8691.
(48) Chaban, V. V.; Prezhdo, V. V.; Prezhdo, O. V. *J. Phys. Chem. Lett.* **2013**, *4*, 1−6.
(49) Kilin, D. S.; Tsemekhman, K. L.; Kilina, S. V.; Balatsky, A. V.; Prezhdo, O. V. *J. Phys. Chem. A* **2009**, *113*, 4549−4556.
(50) Long, R.; English, N. J.; Prezhdo, O. V. *J. Am. Chem. Soc.* **2013**, *135*, 18892−18900.
(51) Long, R.; Prezhdo, O. V. *Nano Lett.* **2014**, *14*, 3335−3341.
(52) Akimov, A. V.; Asahi, R.; Jinnouchi, R.; Prezhdo, O. V. *J. Am. Chem. Soc.* **2015**, *137*, 11517−11525.
(53) Long, R.; Prezhdo, O. V. *Nano Lett.* **2015**, *15*, 4274−4281.
(54) Long, R.; Prezhdo, O. V. *Nano Lett.* **2016**, *16*, 1996−2003.
(55) Akimov, A. V.; Prezhdo, O. V. *J. Chem. Theory Comput.* **2013**, *9*, 4959−4972.
(56) Jasper, A. W.; Nangia, S.; Zhu, C.; Truhlar, D. G. *Acc. Chem. Res.* **2006**, *39*, 101−108.
(57) Baer, R.; Neuhauser, D. *J. Chem. Phys.* **2004**, *121*, 9803−9807.
(58) Kohn, W.; Sham, L. J. *Phys. Rev.* **1965**, *140*, A1133−A1138.
(59) Isborn, C. M.; Li, X.; Tully, J. C. *J. Chem. Phys.* **2007**, *126*, 134307.
(60) Hammes-Schiffer, S.; Tully, J. C. *J. Chem. Phys.* **1994**, *101*, 4657−4667.
(61) Sparpaglione, M.; Mukamel, S. *J. Phys. Chem.* **1987**, *91*, 3938−3943.
(62) Newton, M. D.; Sutin, N. *Annu. Rev. Phys. Chem.* **1984**, *35*, 437−480.
(63) Mead, C. A.; Truhlar, D. G. *J. Chem. Phys.* **1982**, *77*, 6090−6098.
(64) Henderson, M. A. *Surf. Sci. Rep.* **2011**, *66*, 185−297.
(65) Ardo, S.; Meyer, G. J. *Chem. Soc. Rev.* **2009**, *38*, 115−164.
(66) Cave, R. J.; Newton, M. D. *Chem. Phys. Lett.* **1996**, *249*, 15−19.
(67) Smith, F. T. *Phys. Rev.* **1969**, *179*, 111.
(68) Kresse, G.; Furthmüller, J. *Phys. Rev. B: Condens. Matter Mater. Phys.* **1996**, *54*, 11169−11186.
(69) Kresse, G.; Hafner, J. *Phys. Rev. B: Condens. Matter Mater. Phys.* **1993**, *47*, 558−561.
(70) Perdew, J. P.; Burke, K.; Ernzerhof, M. *Phys. Rev. Lett.* **1996**, *77*, 3865−3868.
(71) Lieb, E. H.; Oxford, S. *Int. J. Quantum Chem.* **1981**, *19*, 427−439.
(72) Levy, M. *Int. J. Quantum Chem.* **1989**, *36*, 617−619.
(73) Blöchl, P. E. *Phys. Rev. B: Condens. Matter Mater. Phys.* **1994**, *50*, 17953−17979.
(74) Kresse, G.; Joubert, D. *Phys. Rev. B: Condens. Matter Mater. Phys.* **1999**, *59*, 1758−1775.
(75) Calzado, C. J.; Hernández, N. C.; Sanz, J. F. *Phys. Rev. B: Condens. Matter Mater. Phys.* **2008**, *77*, 045118.
(76) Liu, C.; Kong, D.; Hsu, P.-C.; Yuan, H.; Lee, H.-W.; Liu, Y.; Wang, H.; Wang, S.; Yan, K.; Lin, D.; Maraccini, P. A.; Parker, K. M.; Boehm, A. B.; Cui, Y. *Nat. Nanotechnol.* **2016**, *11*, 1098−1104.
(77) Grimme, S. *J. Comput. Chem.* **2006**, *27*, 1787−1799.
(78) Liu, Y. *Acta Chim. Sinica* **2013**, *71*, 260−264.
(79) Pal, S. K.; Sundstrom, V.; Galoppini, E.; Persson, P. *Dalton Trans.* **2009**, 10021−10031.
(80) Ferrari, A. C. *Solid State Commun.* **2007**, *143*, 47−57.
(81) Casiraghi, C.; Hartschuh, A.; Qian, H.; Piscanec, S.; Georgi, C.; Fasoli, A.; Novoselov, K. S.; Basko, D. M.; Ferrari, A. C. *Nano Lett.* **2009**, *9*, 1433−1441.
(82) Guo, X.-Y.; Xu, D.-P.; Ding, Z.-H.; Su, W.-H. *Chin. Phys. Lett.* **2006**, *23*, 1645.
(83) Baumard, J.-F.; Gervais, F. *Phys. Rev. B* **1977**, *15*, 2316−2323.
(84) Zhugayevych, A.; Tretiak, S. *Annu. Rev. Phys. Chem.* **2015**, *66*, 305−330.
(85) Athanasopoulos, S.; Hoffmann, S. T.; Bassler, H.; Kohler, A.; Beljonne, D. *J. Phys. Chem. Lett.* **2013**, *4*, 1694−1700.
(86) Li, Y. H.; Artes, J. M.; Qi, J.; Morelan, I. A.; Feldstein, P.; Anantram, M. P.; Hihath, J. *J. Phys. Chem. Lett.* **2016**, *7*, 1888−1894.
(87) Kirk, M. L.; Shultz, D. A. *Coord. Chem. Rev.* **2013**, *257*, 218−233.
(88) Johansson, P. G.; Kopecky, A.; Galoppini, E.; Meyer, G. J. *J. Am. Chem. Soc.* **2013**, *135*, 8331−8341.
(89) Liu, Y. Z.; Persson, P.; Sundstrom, V.; Warnmark, K. *Acc. Chem. Res.* **2016**, *49*, 1477−1485.
(90) Lui, C. H.; Mak, K. F.; Shan, J.; Heinz, T. F. *Phys. Rev. Lett.* **2010**, *105*, 127404.

DOI: 10.1021/jacs.6b09598
J. Am. Chem. Soc. 2017, 139, 2619−2629